

WEIBEL INSTABILITY IN HOT PLASMA FLOWS WITH PRODUCTION OF GAMMA-RAYS AND ELECTRON-POSITRON PAIRS

E. N. NERUSH,¹ D. A. SEREBRYAKOV,¹ AND I. YU. KOSTYUKOV¹

¹*Institute of Applied Physics of the Russian Academy of Sciences, 46 Ulyanov St., Nizhny Novgorod 603950, Russia*

Submitted to ApJ

Abstract

We present the results of theoretical analysis and numerical simulations of the Weibel instability in two counter-streaming hot relativistic plasma flows, e.g. flows of electron-proton plasma having rest-mass density $\rho \sim 10^{-4} \text{ g cm}^{-3}$, Lorentz factors $\Gamma \sim 10$ and proper temperature $T \sim 10^{13} \text{ K}$. The instability growth rate and the filament size at the linear stage are found analytically, and are in qualitative agreement with results of three-dimensional particle-in-cell simulations. In the simulations, incoherent synchrotron emission and pair photoproduction in electromagnetic fields are taken into account. If the plasma flows are dense, fast and/or hot enough, the overall energy of synchrotron photons can be much larger than the energy of generated electromagnetic fields. Furthermore, a sizable number of positrons can be produced due to the pair photoproduction in the generated magnetic field. We propose a rough criterion for judging copious pair production and synchrotron losses. By means of this criterion we conclude that incoherent synchrotron emission and pair production during the Weibel instability can have implications for the collapsar model of gamma-ray bursts.

Keywords: gamma-ray burst: general — instabilities — methods: numerical — shock waves

arXiv:1709.05566v1 [astro-ph.HE] 16 Sep 2017

1. INTRODUCTION

The Weibel instability (Weibel 1959) is thought to be a source of near-equipartition magnetic field and a power-law high-energy tail in electron spectra (Silva et al. 2003; Saito & Sakai 2004; Spitkovsky 2008; Nishikawa et al. 2009) in a plenty of astrophysical objects, e.g. in gamma-ray bursts (GRBs). The magnetic field lives for a long time due to nonlinear growth of the field scale (Silva et al. 2003; Medvedev et al. 2005) or even longer due to continuous particle injection (Garasev & Derishev 2016), and ensures prolonged synchrotron emission needed for GRBs afterglow interpretation (Piran 1999). Synchrotron afterglow model explains the GRB emission fairly well at least in radio band (Chevalier 1998; Soderberg et al. 2010). The Weibel instability have been intensively studied theoretically (Grassi et al. 2017), numerically (including extreme laser fields, see Efimenko et al. (2017)) and experimentally (Liu et al. 2011; Huntington et al. 2015; Garasev et al. 2017).

One may notice that the power of the synchrotron emission is proportional to (Landau & Lifshitz 1975) $\gamma^2 B^2$, where γ is the electron Lorentz factor and B is the magnitude of the large-scale electromagnetic fields. Thus, this power is approximately proportional to the cube of the energy density of the flows Piran (1999), and the energy being carried away by synchrotron photons can become greater than the energy of large-scale electromagnetic fields for quite dense and energetic flows. More precisely, we consider plasmas and fields such that $\chi \sim 1$, where χ is the quantum parameter crucial for synchrotron emission (Berestetskii et al. 1982):

$$\chi = \frac{e\hbar}{m^3 c^4} \sqrt{(\varepsilon E/c + \mathbf{p}_e \times \mathbf{B})^2 - (\mathbf{p}_e \cdot \mathbf{E})^2}, \quad (1)$$

where ε and \mathbf{p}_e are the electron energy and momentum, \mathbf{E} and \mathbf{B} are the electric and magnetic field magnitudes, \hbar is the Planck's constant, c is the speed of light, $e > 0$ and m are the electron charge and mass, respectively. If $\chi \gtrsim 1$, the energy of a photon emitted by an electron is about the electron energy, and the average distance on which the photon emission occurs is about $\ell_{em} \sim \ell_f/\alpha$, where $\ell_f \sim mc^2/(eB)$ is the radiation formation length (Berestetskii et al. 1982) and $\alpha = e^2/\hbar c \approx 1/137$ is the fine structure constant. Hence the ratio of ℓ_{em}/c to the timescale of the Weibel instability (Grassi et al. 2017) is the following:

$$\frac{\ell_{em}\omega}{c\bar{\gamma}_e^{1/2}} \sim \frac{1}{\alpha\bar{\gamma}_e}, \quad (2)$$

where $\omega = (4\pi e^2 n_e/m)^{1/2}$ is the electron plasma frequency, and we use the equipartition assumption $B^2 \sim$

$8\pi n_e m c^2 \bar{\gamma}_e$, n_e is the electron density, $\bar{\gamma}_e$ is the mean electron Lorentz factor. Eq. (2) obviously means that if $\bar{\gamma}_e \gtrsim 137$ and $\chi \sim 1$ is reached, the synchrotron emission potentially can take away the electron energy in a timescale lower than the Weibel instability timescale. Thus, synchrotron losses should be taken into account if one considers the Weibel instability in dense ultrarelativistic plasma flows.

If for an electron $\chi \sim 1$, it quite probably emits a photon with momentum $p_\gamma \sim p_e$ almost parallel to the electron momentum, $\mathbf{p}_\gamma \parallel \mathbf{p}_e$ and with the energy about the electron energy (Baier et al. 1998; Berestetskii et al. 1982), $\varepsilon_\gamma \sim \varepsilon$. Pair photoproduction in strong electromagnetic field:

$$\gamma \rightarrow e^+ + e^- \quad (3)$$

is governed by the quantum parameter

$$\varkappa = \frac{e\hbar}{m^3 c^4} \sqrt{(\varepsilon_\gamma E/c + \mathbf{p}_\gamma \times \mathbf{B})^2 - (\mathbf{p}_\gamma \cdot \mathbf{E})^2}, \quad (4)$$

that is the same as χ (Eq. (1)) with ε_γ and \mathbf{p}_γ substituted for ε and \mathbf{p}_e , respectively. Hence, for the photon emitted by electron with $\chi \gtrsim 1$, we estimate $\varkappa \gtrsim 1$. In this case, the probability of the pair photoproduction is of the order of the probability of emission of synchrotron photon by the electron. Therefore, pair production (3) should be also taken into account, that can be done by means of Monte Carlo technique Nerush et al. (2014) utilizing Baier–Katkov quasiclassical formulas (Baier et al. 1998; Berestetskii et al. 1982).

Here we present the results of numerical simulations of the Weibel instability in two counter-streaming hot and dense relativistic plasma flows. Unlike synchrotron emission and pair production, particle collisions (e.g., Compton scattering and bremsstrahlung) are not included in the simulations.

Let us also note that in the theoretical considerations of the Weibel instability we follow electromagnetic scenario (Stockem et al. 2014), because for ultrarelativistic flows ($\Gamma \gg 1$, where Γ is the Lorentz factor of a flow in some, e.g. in the laboratory, reference frame K), almost all velocity vectors of plasma particles belong to a cone $\theta \lesssim 1/\Gamma$ despite a high temperature of the flow (see Fig. 1; here θ is the angle between the particle velocity and the flow velocity). This is true even if the average Lorentz factor of the flow particles in the comoving reference frame K' is much greater than Γ , that is evident from the Lorentz transform of angles from the proper reference frame of the flow K' to K :

$$\tan \theta = \frac{v'_x}{\Gamma(v'_x + V)} \tan \theta', \quad (5)$$

where V is the flow velocity in K and the x axis is parallel to it. Furthermore, it follows from the transformation

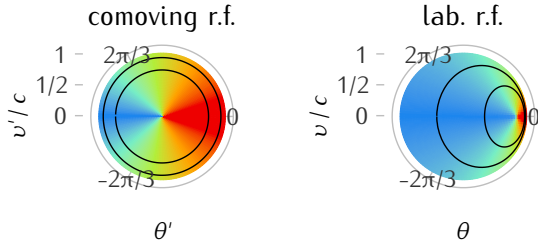


Figure 1. The distribution of the azimuth θ' in the proper reference frame of the flow (K' , left) and in the laboratory reference frame (K , right) (different values of θ' are shown with different colors; radial coordinate depicts velocity v). $\theta' = 0$ corresponds to the direction of the relative velocity V of the reference frames; for this plot $V = 0.86c$.

of the Lorentz factor:

$$\gamma = \gamma' \Gamma (1 + v'_x V), \quad (6)$$

that the proper temperature of the flow determines the mean energy of particles in the laboratory reference frame, $\bar{\gamma} = \bar{\gamma}' \Gamma$ (we assume $\bar{v}'_x = 0$). Therefore, a hot plasma flow with $\Gamma \gg 1$ should behave similarly to a cold plasma flow, and the Weibel instability in the counter-streaming flows should grow in accordance with the electromagnetic scenario (formation and growth of current filaments with azimuthal magnetic field and low electric field, see [Stockem et al. \(2014\)](#); [Garasev et al. \(2017\)](#) and references therein) rather than with the electrostatic one.

The paper is organized as follows. In Sec. 2.1, we consider the Weibel instability of the electromagnetic type in counter-streaming relativistically hot plasma flows analytically, without synchrotron emission and pair production. In Sec. 2.2, we estimate the plasma parameters corresponding to $\chi \sim 1$ and $\varkappa \sim 1$, hence, efficient synchrotron emission and copious pair production. In Sec. 3, the results of numerical simulations with synchrotron emission and pair production taken into account are given, and in Sec. 4, their astrophysical implications are discussed. In Sec. 5, the summary of the paper is given.

2. WEIBEL INSTABILITY IN HOT COLLISIONLESS PLASMAS

2.1. Effect of temperature

Let us consider the stability of two relativistic counter-propagating plasma flows moving along the x axis, with respect to the formation of a cylindrically symmetric current filament. The properties of the flows are further denoted by indices 1 (the flow velocity $v_x > 0$) and 2

($v_x < 0$). We also assume that the filament remains quasineutral and

$$\delta n_{e1} = \delta n_{i2} = -\delta n_{i1} = -\delta n_{e2}, \quad (7)$$

where δn is the density perturbation relative to the initial value for the flow (n_1 or n_2), the indices i and e refer to protons and electrons, respectively (the assumption (7) will be justified a bit later, it is not always fulfilled and is used to simplify calculations). Let r and φ be the cylindrical coordinates with respect to the axis of the current filament coinciding with the x axis. x , r and φ are right-handed coordinates. We also assume that none of the plasma characteristics depend on x , therefore the Maxwell's equations can be written as follows:

$$\frac{\partial E_x}{\partial t} = \frac{c}{r} \frac{\partial(rB_\varphi)}{\partial r} + 16\pi e c \delta n_{e1}, \quad (8)$$

$$\frac{\partial B_\varphi}{\partial t} = c \frac{\partial E_x}{\partial r}. \quad (9)$$

To obtain the equation for the density perturbation, one should start from the Boltzmann equation in Cartesian coordinates:

$$\frac{\partial f}{\partial t} + (\mathbf{v}, \nabla) f + \frac{(\mathbf{F}, \nabla_{\mathbf{v}})}{m\gamma} f = 0 \quad (10)$$

where $f(r, \mathbf{v})$ is the distribution function, $\gamma = (1 - v^2)^{1/2}$, and we assume that for particles $\mathbf{F} \perp \mathbf{v}$ hence $d\gamma/dt = 0$. Here the boldly denoted vectors are in the $y - z$ plane, perpendicular to the x axis. For particle density

$$n(y, z) = \iiint_{v^2 < c^2} f(y, z, v_x, v_y, v_z) dv_x dv_y dv_z \quad (11)$$

from the Boltzmann equation we obtain

$$\frac{\partial \bar{n}}{\partial t} = -\nabla \cdot (n \bar{\mathbf{v}}), \quad (12)$$

where the bar denotes averaging over velocities:

$$\bar{a} = \frac{1}{n} \iiint_{v^2 < c^2} a f dv_x dv_y dv_z. \quad (13)$$

For the average velocity we obtain

$$\frac{\partial \bar{v}_k}{\partial t} = \left(\frac{F_k}{m\gamma} \right) - \bar{v}_l \frac{\partial \bar{v}_k}{\partial x_l} - \frac{1}{n} \frac{\partial}{\partial x_l} \left[\overline{(v_l - \bar{v}_l)(v_k - \bar{v}_k)} n \right], \quad (14)$$

where Einstein summation convention is used. We also assume that the covariance matrix for \mathbf{v} is a constant, i.e.

$$\mathcal{V}_{kl} \equiv \overline{(v_k - \bar{v}_k)(v_l - \bar{v}_l)} = \text{const}, \quad (15)$$

and the distribution function is assumed to be symmetrical in the yz coordinates, so that $\mathcal{V}_{k \neq l} = 0$ and $\mathcal{V}_{zz} = \mathcal{V}_{yy} \equiv \mathcal{V}$. Then the equation (14) for v_y or v_z can be written as

$$\frac{\partial \bar{v}_k}{\partial t} = \overline{\left(\frac{F_k}{m\gamma} \right)} - \bar{v}_l \frac{\partial \bar{v}_k}{\partial x_l} - \frac{\mathcal{V}}{n} \frac{\partial n}{\partial x_k}. \quad (16)$$

We suppose that in the case of a relativistically hot plasma in the proper reference frame, the plasma particles are uniformly distributed over the surface of a sphere $v_x'^2 + v_y'^2 + v_z'^2 \simeq c^2$, hence, using velocity transformation formulas

$$v_x = \frac{v_x' + V}{1 + v_x'V/c^2} \quad (17)$$

$$v_{y,z} = \frac{v_{y,z}' \sqrt{1 - V^2/c^2}}{1 + v_x'V/c^2}, \quad (18)$$

one may easily derive the expression for \mathcal{V} in the reference frame where the flow velocity is relativistic:

$$\begin{aligned} \mathcal{V} &\simeq \frac{1}{\Gamma^2} \iint_{v_y'^2 + v_z'^2 < c^2} \frac{v_y'^2}{v_x'(1 + v_x'/c)^2} dv_y' dv_z' \\ &\times \left(\iint_{v_y'^2 + v_z'^2 < c^2} \frac{1}{v_x'} dv_y' dv_z' \right)^{-1} \approx \frac{0.2c^2}{\Gamma^2}. \end{aligned} \quad (19)$$

Here $v_x' = (c^2 - v_y'^2 - v_z'^2)^{1/2}$.

After that, the equations (12) and (16) can be rewritten in cylindrical coordinates, assuming that $\bar{v}_\varphi = 0$:

$$\frac{\partial n}{\partial t} = -\frac{1}{r} \frac{\partial (rn\bar{v}_r)}{\partial r}, \quad (20)$$

$$\frac{\partial \bar{v}_r}{\partial t} = \overline{\left(\frac{F_r}{m\gamma} \right)} - \bar{v}_r \frac{\partial \bar{v}_r}{\partial r} - \frac{\mathcal{V}}{n} \frac{\partial n}{\partial r}. \quad (21)$$

We consider only the initial stage of the instability, so for the force in Eq. (21) the following expression can be used:

$$\bar{F}_r \simeq \pm eB_\varphi, \quad (22)$$

where the sign is determined by the sign of \bar{v}_x and the sign of the particle charge, hence we can estimate

$$\overline{\left(\frac{F_r}{m\gamma} \right)} \simeq \frac{F_r}{m\gamma}. \quad (23)$$

It can be noted that the sign of the force is the same for the ions (electrons) of the first flow and electrons (ions) of the second flow, so in the case of flows with the same parameters (density, Lorentz factor and temperature) the density is perturbed such that the quasineutrality condition (7) stands true. Otherwise, when densities or

Lorentz factors of the flows do not coincide, the condition (7) may not be fulfilled, but we will use it for the sake of simplicity, assuming the plasma is quasi-neutral.

We look for the solution of the Maxwell's equations (8), (9) together with the equations (20), (21) in the following form:

$$E_x = E_0 e^{\Lambda t} J_0(r/\lambda), \quad (24)$$

$$\delta n_{e1} = -\delta n_0 e^{\Lambda t} J_0(r/\lambda), \quad (25)$$

$$v_r \propto B_\varphi \propto e^{\Lambda t} \frac{dJ_0(r/\lambda)}{dr}, \quad (26)$$

where E_0 and δn_0 are the amplitudes, J_0 is the zero-order Bessel function of the first kind, i.e. the solution of the equation

$$\frac{1}{r} \frac{d}{dr} \left\{ r \frac{d[rJ_0(r/\lambda)]}{dr} \right\} = -\frac{1}{\lambda^2} J_0(r/\lambda). \quad (27)$$

Therefore, we obtain the equations which describe the parameters of cylindrically-symmetric modes:

$$\left(1 - \frac{4\omega_1^2}{\bar{\gamma}_1 \Lambda^2} \right) \frac{c^2}{\lambda^2} E_0 + \Lambda^2 E_0 + \frac{16\pi e c \mathcal{V}_1}{\Lambda \lambda^2} \delta n_0 = 0, \quad (28)$$

$$\frac{\mathcal{V}_1}{\lambda^2} \delta n_0 - \frac{n_1 e c}{\Lambda m \bar{\gamma}_1} \frac{1}{\lambda^2} E_0 + \Lambda^2 \delta n_0 = 0, \quad (29)$$

where n_1 , again, is the first flow initial density $n_1 \equiv n_{e,1}(t=0)$ and $\omega_1^2 = 4\pi e^2 n_1/m$ is the related plasma frequency.

The first equation at $\mathcal{V} = 0$ describes, in addition to the stable mode, the Weibel instability, and the second at $E_0 = 0$ describes quasi-sound waves. In the first and second cases, it is easy to obtain a relation between the characteristic spatial scale of the mode λ and the characteristic "increment" Λ :

$$\Lambda_{\mathcal{V}=0}^2 = \frac{c^2}{2\lambda^2} \left(-1 \pm \sqrt{1 + \frac{16\lambda^2 \omega_1^2}{c^2 \bar{\gamma}_1}} \right), \quad (30)$$

$$\Lambda_{E_0=0}^2 = -\frac{\mathcal{V}_1}{\lambda^2}. \quad (31)$$

The relation between Λ and λ can be found from the equations (30) and (31) in the general case as well:

$$\Lambda^4 + \frac{c^2 + \mathcal{V}_1}{\lambda^2} \Lambda^2 - \frac{c^2}{\lambda^2} \left(\frac{4\omega_1^2}{\bar{\gamma}_1} - \frac{\mathcal{V}_1}{\lambda^2} \right) = 0, \quad (32)$$

therefore, taking into account that $\mathcal{V}_1 \ll c^2$, we derive for the unstable mode

$$\Lambda^2 = \frac{c^2}{2\lambda^2} \left(-1 + \sqrt{1 + \frac{4\lambda^2}{c^2} \left(\frac{4\omega_1^2}{\bar{\gamma}_1} - \frac{\mathcal{V}_1}{\lambda^2} \right)} \right). \quad (33)$$

In the above equation it can be seen that at $\mathcal{V} \neq 0$ the considered mode is unstable ($\Lambda^2 > 0$) if

$$\lambda > \frac{\sqrt{\bar{\gamma}_1 \mathcal{V}_1}}{2\omega_1}, \quad (34)$$

i.e., for modes with a spatial scale, greater than some. It can be easily shown that in the presence of temperature the maximum increment Λ_m is realized for the mode with the following spatial scale:

$$\lambda_m^2 \sim \mathcal{V}_1 \bar{\gamma}_1 / \omega_1^2, \quad \frac{\lambda_m}{\lambda_1} \sim \frac{1}{2\pi} \frac{\bar{\gamma}_1^{1/2}}{\Gamma_1}, \quad (35)$$

and equals

$$2\pi\Lambda_m/\omega_1 \sim 2\pi/\sqrt{\bar{\gamma}_1}. \quad (36)$$

Note that although we obtain Eqs. (35) and (36) for the flows with equal parameters, we will use these equations for the flows with different parameters as well, assuming that the index 1 denotes the flow with higher corrected plasma frequency: $\omega_1/\bar{\gamma}_1^{1/2} > \omega_2/\bar{\gamma}_2^{1/2}$ that yields higher value for the increment (36). The obtained estimates are compared with results of numerical simulations in Sec. 3.

2.2. Pair production

Here we consider pair photoproduction (3) in the electromagnetic fields during the Weibel instability. The pair production becomes efficient if $\varkappa \gtrsim 1$, where the quantum parameter \varkappa depends on the field magnitude and the energy of the photon (4). In order to check if the process (3) appears in some astrophysical objects, the magnitude of electromagnetic fields and photon energy should be found.

For the sake of simplicity we consider the Weibel instability in two counter-streaming plasma flows in the reference frame where the momentum flow is the same for both jets:

$$n_1\Gamma_1 V_1^2 \eta_1 \simeq n_2\Gamma_2 V_2^2 \eta_2. \quad (37)$$

Here we estimate $\bar{\gamma}_1 \approx \Gamma_1 \eta_1$ and $\bar{\gamma}_2 \approx \Gamma_2 \eta_2$. The parameter η defines the average kinetic energy of ions in the reference frame comoving with the flow as follows:

$$\eta = \overline{(\gamma_i - 1)}. \quad (38)$$

From here on we assume that flow 1 is denser than flow 2 ($n_1 > n_2$), and in flow 2, ions and electrons are more energetic than in flow 1 ($\bar{\gamma}_2 \gtrsim \bar{\gamma}_1$).

We assume that a sizable part of the initial energy of the flows is transferred to the energy of electromagnetic fields, and the magnitude of the fields can be estimated as follows:

$$B^2 \sim 8\pi n_2 m c^2 \bar{\gamma}_2, \quad (39)$$

where we additionally suppose that the volume occupied by the plasma is not changed much while the filaments grow. An electron in strong enough fields emits photons with energy about its own energy (namely if $\chi \gtrsim 1$, see Sec. 1). Therefore, in \varkappa (Eq. 4) we can estimate the photon energy as follows

$$\varepsilon_\gamma \sim m c^2 \bar{\gamma}_2, \quad (40)$$

that leads to

$$\varkappa \sim \bar{\gamma}_2^{3/2} \sqrt{8\pi n_2 r_e \lambda_C^2}, \quad (41)$$

where $r_e = e^2/(mc^2)$ is the classical electron radius and $\lambda_C = \hbar/mc$ is the Compton wavelength. Supposing that the average electron energy initially or after the acceleration process (Silva et al. 2003; Spitkovsky 2008) is as high as the initial ion energy, we have $\bar{\gamma}_2 \approx \Gamma_2 \eta_2 M/m$. Therefore, copious pair production is ensured if

$$\varkappa \sim (\eta_2 \Gamma_2 M/m)^{3/2} \sqrt{8\pi n_2 r_e \lambda_C^2} \gtrsim 1. \quad (42)$$

Here, again, all values are given in the center-of-momentum reference frame (37) and the index 2 denotes the flow whose particle density is lower than the density of the other.

In the case of strong synchrotron losses the equipartition assumption can lead to an overestimation of the fields magnitude. On the other hand, we estimate the photon energy using the mean particle energy and not taking into account high-energy spectrum tails (Silva et al. 2003; Spitkovsky 2008). Thus, the resulting criterion of copious pair production Eq. (42) remains relevant, as shown in the next Section by means of numerical simulations.

3. RESULTS OF NUMERICAL SIMULATIONS

To verify the above estimates, we performed three-dimensional numerical simulations of the development of the Weibel instability in counter-propagating hot plasma flows using the particle-in-cell (PIC) code QUILL (Nerush & Kostyukov 2010; Serebryakov et al. 2015). The simulations were carried out taking into account emission of hard photons and pair photoproduction in a strong field using the Monte Carlo method (Elkina et al. 2011; Nerush et al. 2014). Collisions of particles and, in particular, Compton scattering and bremsstrahlung are not taken into account. To solve the Maxwell equations and to approximate currents and fields, we used algorithms of Pukhov (1999), to solve the equations of motion we used the method of Vay (2008).

We chose the following simulation parameters: the size of the simulation region was $54 \times 24 \times 24 \lambda_1^3$, where λ_1 ,

as before, is the plasma wavelength of the denser flow. Initially each of the flows occupied half of the region. The transverse step of the numerical grid was equal to $\Delta y = \Delta z = 0.14 \lambda_1$, the longitudinal one was $\Delta x = 0.063 \lambda_1$, the time step was $\Delta t = 0.06 \times 2\pi/\omega_1$. The initial number of quasiparticles of each species (electrons and ions) in a cell was equal to 8. The quasiparticle merging algorithm was not used. The plasma density of the flows had a flat transverse profile with a decrease in the density at the edges to zero on the scale $\sim 2 \lambda_1$. We used open boundary conditions that allowed the free outflow of the electromagnetic waves and particles at the boundaries (Pukhov 1999).

Initially, the particles of the flow in the comoving reference frame had the distribution:

$$f_i \propto e^{-(\gamma-1)/\eta}, \quad (43)$$

$$f_e \propto e^{-m(\gamma-1)/(M\eta)}, \quad (44)$$

hence the average kinetic energy of the ions (or the electrons) in the comoving reference frame was equal to $Mc^2\eta$.

We have carried out a series of seven simulations for different Lorentz factors, densities and temperatures of the plasma flows. The simulation parameters are given in Table 1, where s^* means the simulation identifier. The proton to electron mass ratio M/m in the simulations was chosen much lower than that for the real particles in order to reduce computational costs. For the given parameters of the simulations the instability growth rate Λ_m and the transverse scale of the filaments λ_m were computed with Eqs. (36) and (35), respectively. The parameter \varkappa crucial for the pair photoproduction was estimated with Eq. (41). In most simulations, the end time was equal to $t_{end} = 27 \times 2\pi/\omega_1$. However, in some simulations we were forced to terminate them before t_{end} due to the significant growth of the number of particles (mostly photons). In those simulations, the end time is given as a subscript in a simulation identifier (e.g., $s4_{22}$). The ratio of the number of positrons to the number of electrons N_p/N_e at the end of a simulation and the quantity dN_p/dN_γ characterizing the positron generation efficiency (see more details further) are computed in the simulations and are also given in the Table 1.

Let us consider $s2$ simulation as an example. Fig. 2 (a) shows the sum electron and ion density (as color intensity) as well as the relative electric charge (shown as color hue) at the filaments cross-section. It is seen that plasma remains close to neutral during the instability growth. Fig. 2 (b) depicts the transverse (azimuthal) magnetic field generated around the filaments. It should be noted that the typical filament size and the scale

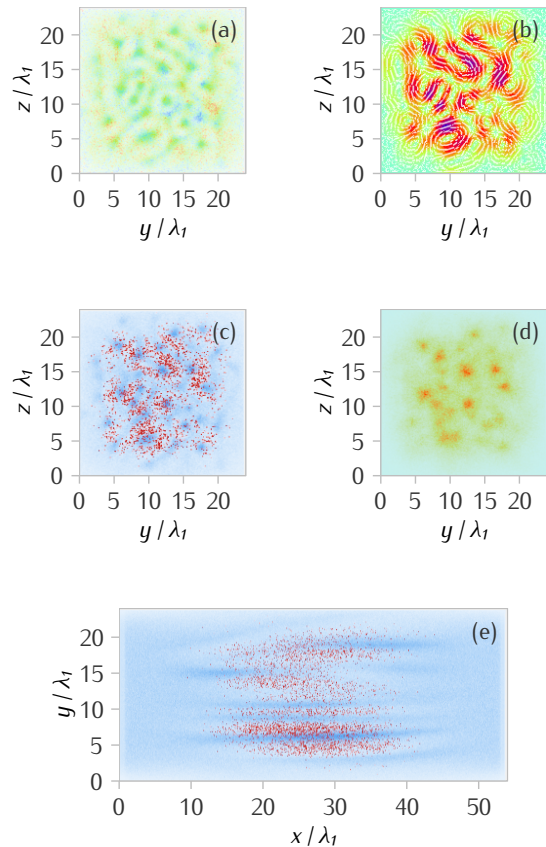
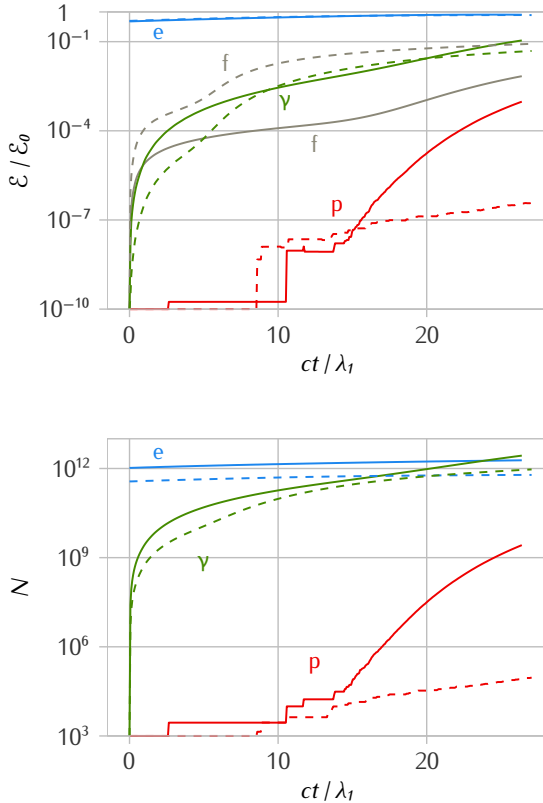


Figure 2. The results of $s2$ simulation. (a) In the $y-z$ plane, the total proton and electron density shown with the color intensity, the ratio of the charge density to the total particle density depicted by the color hue (red color corresponds to a plasma consisting of 60% ions and 30% electrons, blue color corresponds to 30% ions and 60% electrons mixture). (b) The transverse magnetic field energy density ($B_y^2 + B_z^2$) distribution in the $y-z$ plane, the darker colors correspond to the higher energy density, white lines sketchily show the field direction. The electron (blue) and positron (red) density distribution in (c) yz and (e) the $x-y$ planes, respectively. Note that the maximum positron density is about 2 orders of magnitude lower than that of electrons. (d) The gamma quanta density in the $y-z$ plane. All distributions are given at the time instant $t = 26\lambda_1/c$. Both the $x-y$ plane and the $y-z$ plane pass through the center of the simulation area.

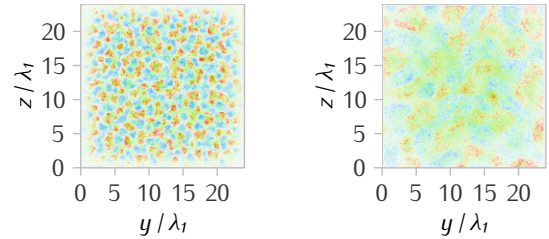
of the magnetic field they generate is approximately of the order of the distance between the filaments. From Figs. 2 (c) and (d) showing electron and photon density distributions, respectively, one can see that the positions of these distributions maximums coincide. At the same time, the distribution of the generated positrons is similar to the distribution of the magnetic field (see Figs. 2 (b), (c) and (e)).

Table 1. Simulation parameters and results.

Simulation	n_1 (cm^{-3})	η_1	Γ_1	n_2/n_1	η_2	Γ_2	M/m	λ_m/λ_1	$2\pi\Lambda_m/\omega_1$	\varkappa	N_p/N_e	dN_p/dN_γ
s1	1×10^{25}	2	25	0.25	20	10	10	0.14	0.28	14	1.4×10^{-3}	6×10^{-3}
s2 ₂₆	6.3×10^{23}	20	10	1	20	10	10	0.71	0.14	7.2	1.4×10^{-3}	3×10^{-3}
s3	2.5×10^{24}	5	10	0.4	5	25	1	0.11	0.89	0.14	1.5×10^{-7}	$< 10^{-6}$
s4 ₂₂	1.6×10^{23}	1.3	10	1	1.3	10	15	0.22	0.45	0.11	1.4×10^{-8}	$< 10^{-6}$
s5	7.7×10^{22}	10	16	0.5	2	160	15	0.49	0.13	6.5	7×10^{-6}	7×10^{-5}
s6 ₂₃	1.9×10^{22}	7	4	0.7	4	10	20	0.94	0.27	0.27	3.6×10^{-9}	$< 10^{-6}$
s7	5×10^{24}	2	4	0.08	1.2	80	20	0.5	0.5	5.7	3.8×10^{-6}	1×10^{-4}

**Figure 3.** The normalized particle and field energy (upper plot) and the particle number (lower plot) as functions of time in 2 different simulations: s2 (solid lines) and s3 (dashed lines). Electrons (e), positrons (p), photons (γ) and electromagnetic fields (f) are shown.

In Fig. 3 (top), the growth of the energy of electromagnetic fields, the energy of photons and positrons in the process of instability development in s2 simulation is shown with solid lines (for comparison, the dashed

**Figure 4.** The total electron and ion density with the relative charge density (as defined in Fig. 2(a)) for s3 simulation at different time instants: $t = 10\lambda_1/c$ (left) and $t = 20\lambda_1/c$ (right).

lines show the same quantities for s3 simulation). Figure 3(bottom) depicts the number of particles in the s2 and s3 simulations as a function of time. Despite the fact that the energy of electromagnetic fields in s3 simulation is higher, the number of positrons produced in it is negligible compared to s2 simulation. It can be seen from Fig. 3 (top) that the growth rate of the plasma fields energy (i.e. the slope of the f lines) depends on time, which is explained by the transition from the linear stage of development of the instability to the nonlinear one. The nonlinear stage is characterized not only by the growth of fields and perturbation of the plasma density, but also by the merging of current filaments. For an example, see the density distribution in the $y-z$ plane for s3 simulation in Fig. 4 at two different time instants.

Consider the entire set of the simulation results (s1–s7). The characteristic transverse scale of the filaments ℓ was found from the simulation results as follows. First, the modulus of the Fourier image of B_y was computed, and the background of it (values below 0.1 of its maximum) was deleted. Fig. 5 (a) shows such a Fourier image

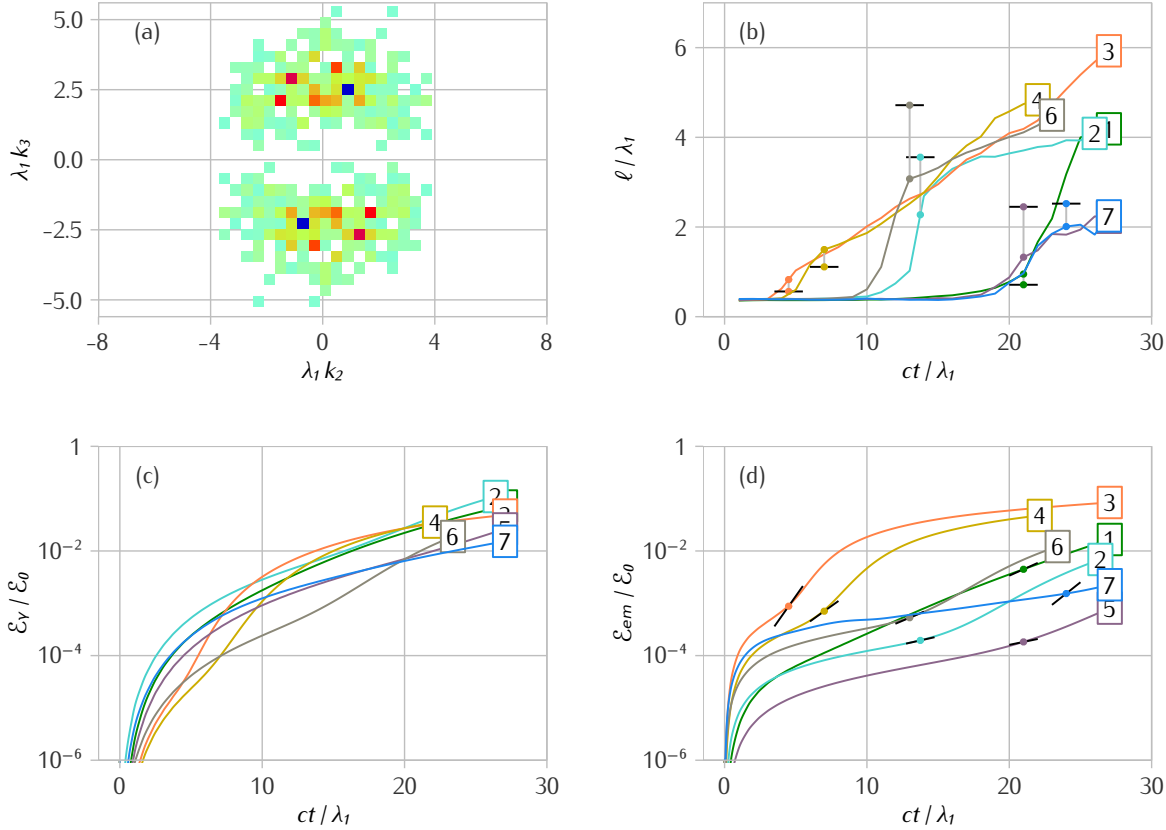


Figure 5. (a) The two-dimensional Fourier image of the magnetic field component $B_y(y, z)$ in the simulation s3 at $t = 10\lambda_1/c$ and x passing the center of the simulation box; k_2 and k_3 are the wavenumbers along the y axis and the z axis respectively. (b) Filament size ℓ for s1–s7 simulations determined from the Fourier images of B_y , as functions of time. Dots mark the time instances at which the evolution turns from linear to nonlinear stage. The ordinate of the black horizontal bars corresponds to the estimate of the filament scale (35) multiplied by 5, i.e. $5\lambda_m/\lambda_1$ (see Table 1 for numerical values). (c) The energy of the gamma-rays and (d) the energy of the large-scale electromagnetic fields normalised to the initial ion energy of the plasma that will fill up the simulation box at the end of the simulation, \mathcal{E}_0 . The short black lines are the exponents $\mathcal{E}_{em} \propto \exp \Lambda_m t$, where Λ_m is the estimate of the instability growth rate (36) (see Table 1 for numerical values).

for s3 simulation and $t = 10\lambda_1/c$. Then, using this image, the dispersion of the transverse wave vectors was computed, for example, Fig. 5 (a) yields the dispersion $k^2 \approx 9.7/\lambda_1^2$ and therefore $\ell = 2\pi/k \approx 2\lambda_1$.

For s1–s7 simulations, the characteristic distance between filaments ℓ computed with this method as function of time is given in Fig. 5 (b). The dependence of the energy of hard photons \mathcal{E}_γ and the dependence of the energy of the electromagnetic field \mathcal{E}_{em} on time are depicted in Figs. 5 (c) and (d), respectively.

In small times, the magnetic field generated due to the Weibel instability is smaller than the noise associated with the temperature, so the described method of filament scale computation in small times gives a scale of the order of the transverse step of the numerical grid. However, if the generated magnetic field becomes greater than the noise level, the sharp growth of

ℓ from these value to some other value occurs. We suppose that the value of ℓ computed at the end of this sharp growth corresponds to filament scale reasonably well. The time instances of this sharp growths and the resulting transverse scales of the filaments for s1–s7 simulations are shown in Fig. 5 (b) with dots, together with the estimated value of the filament size $5\lambda_m$ computed with Eq. (35) and marked with short black lines. We multiplied the analytical values λ_m by 5 for better coincidence between theory and simulations. The need of this multiplier can be explained by the fact that Eq. (35) gives filament radius whereas the method of ℓ computation gives the distance between filaments. Note that the filament size computed for s1 and s3 simulations is close to the step size of the numerical grid, thus, in these simulations the linear stage of the Weibel instability was computed with higher inaccuracy than in the others.

The nonlinear stage of the development of the Weibel instability is characterized, first, by the fact that the density perturbation becomes of the order of the initial particle density and, second, the filament merging. In Fig. 5 (b), almost for all simulations the nonlinear stage starts right after the marked time instances and manifest itself as the subsequent growth of ℓ . By the order of magnitude, the increment at the linear stage of the instability development, obtained in numerical simulation, is in good agreement with the increment estimating by Eq. (36) (see Fig. 5 (d) and Table 1), that does not take into account many factors. For example, in the case of essentially different parameters of the flow 1 and the flow 2, the difference in the density of protons and electrons in filaments can be of the order of the particle density itself (see Fig. 4). In addition, the energy of emitted gamma quanta can significantly exceed the energy of the generated electromagnetic fields even at the initial stage of the instability development (see Fig. 3).

At the saturation of the Weibel instability, in the case of counter streaming plasma flows, the filament current is determined only by the plasma density, and the maximal magnetic field is about $B \sim n_e \ell$. Therefore, the filament size is strongly coupled with the energy of the magnetic field. Therefore, the synchrotron emission should also lead to less filaments radius, because the radiation losses reduce the energy of the magnetic field.

For s2–s6 simulations, a noticeable increase in the instability increment is observed during the transition to the nonlinear stage, but after that the increment can decrease because of the filaments growth and the rise of the characteristic distance between them. It should also be noted that a rapid change in the filament configuration at the nonlinear stage (filament merging) can lead to the appearance of strong electric fields.

Numerical simulations in this work was carried out at the limit of technical capabilities available to the authors. Several calculations were stopped at $t < 27\lambda_1/c$ (until the flows intersected each other completely in the simulation region), because the of the large number of newly-born photons and limited RAM resources. Because of this, the saturation of the Weibel instability was not attained in almost all calculations, however, in all calculations a nonlinear stage of instability was achieved (see Fig. 5). Since the simulation parameters are different and the simulation time is sometimes less than desired, we introduced the parameter $dN_p/dN_\gamma = (dN_p/dt)/(dN_\gamma/dt)$ to isolate the simulations with abundant positron production. This parameter roughly shows the proportion of photons which produce electron-positron pairs. Dependences of the number of positrons and dN_p/dN_γ on time in the s1–s7 sim-

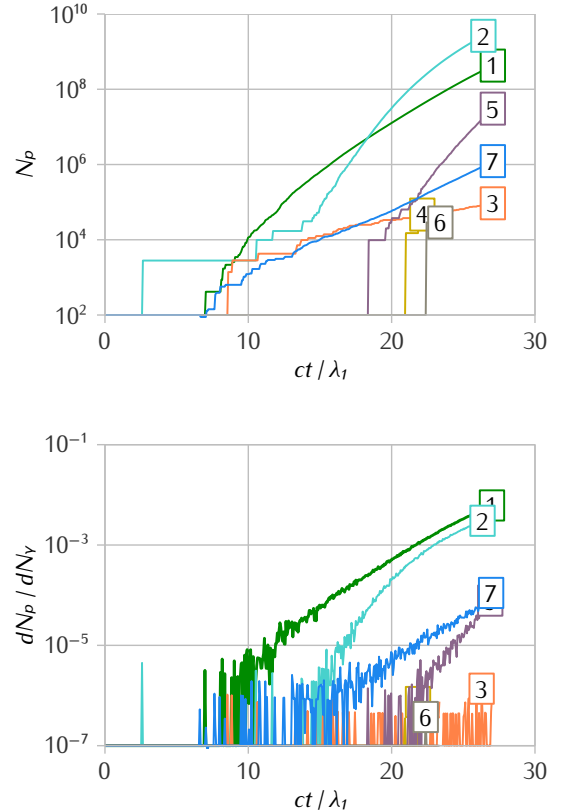


Figure 6. (a) The number of positrons N_p and (b) the parameter dN_p/dN_γ in s1–s7 simulations, as functions of time.

ulations are shown in Figs. 6 (top) and (bottom), respectively. From N_p and dN_p/dN_γ at the end of the simulations (see Table 1), we conclude that in the simulations s1, s2, s5 and s7, a significant production of electron-positron pairs is realized. In the s3, s4 and s6 simulations, a low number of positrons is observed (despite the significant number of the photons), and dN_p/dN_γ does not exceed the background noise values. Thus, the criterion (42), yielding $\varkappa > 1$ for s1, s2, s5 and s7 simulations and $\varkappa < 1$ for s3, s4 and s6 simulations, does indeed allow us to distinguish the pair production regime during the development of the Weibel instability.

4. DISCUSSION AND ASTROPHYSICAL IMPLICATIONS

In this paper, we consider the Weibel instability in two relativistic plasma flows that can lead to the efficient synchrotron emission. The numerical simulations demonstrate that the conversion efficiency of initial flows energy to the energy of synchrotron photons is much higher than that for the generation of large-scale magnetic fields, if the flows are quite dense and energetic.

Numerical simulations also show that the synchrotron photons can produce e^+e^- pairs in the magnetic field, giving the number of positrons up to 10^{-3} and higher of the number of electrons in the flows. In order to clarify the flows parameters leading to copious pair production, the theoretical estimate (42) can be rewritten using the rest-mass density of the hydrogen plasma of the flows ρ (namely the density of the cooled plasma in the comoving reference frame):

$$\varkappa \sim 6.2 \times \eta_2^{3/2} \Gamma_2^2 \sqrt{\rho_2 [\text{g cm}^{-3}]} \gtrsim 1, \quad (45)$$

where the flow Lorentz factors $\Gamma_{1,2}$ are given in the center-of-momentum reference frame (37), $\eta = \overline{(\gamma' - 1)}$ is the mean normalized kinetic energy of the ions in the reference frame comoving with the flow. The index 2 denotes the flow whose particle density is lower than the density of the other, i.e. $n_2 \leq n_1$. For instance, this estimate yields $\varkappa \approx 1$ for $\eta_2 \sim 1$, $\Gamma_2 = 5$ and $\rho_2 \sim 10^{-4} \text{ g cm}^{-3}$.

The simulation results s1–s7 are obtained for M/m far from the real proton-to-electron mass ratio (≈ 1836), but can be scaled in a way that conserves the base estimate (42) as follows: $\eta_2 \Gamma_2$ from Table 1 is multiplied by $aM/(1836m)$, and n_2 is replaced by n_2/a^3 , where a is an arbitrary constant (we choose $a = 10^{4/3}$ in order to fit $\eta_2 \Gamma_2$ in the range 1–100). Values of $\eta_2 \Gamma_2$ and n_2 obtained with this scaling correspond to a hydrogen plasma and can be tested with criterion (45) and compared with believed values of these parameters for astrophysical jets.

The line corresponding to Eq. (45) and $\varkappa \sim 1$ along with points obtained from the simulation results s1–s7, are shown in Fig. 7. Simulations s1, s2, s7 and s5, resulting in high number of positrons and high rate of their production, are marked with red triangles. Simulations s3, s4 and s6, resulting in low number of positrons generated, are marked with green triangles. It is clearly seen that the line $\varkappa \sim 1$ divides well the regions of copious and weak positron production, and Eq. (45) can be used to test various astrophysical objects.

4.1. Gamma-ray bursts

Dense relativistic plasma jets are often associated with gamma-ray bursts (GRBs), tidal disruption events, active galactic nucleus and blazars. The energy of particles in the jets and the jet mass density could not be measured directly, however, the values used in a number of models of this phenomena can be used.

In the collapsar model of MacFadyen & Woosley (MacFadyen & Woosley 1999; Woosley & MacFadyen 1999), GRBs are linked with rotating massive stars whose core collapse produces black hole swallowing surround-

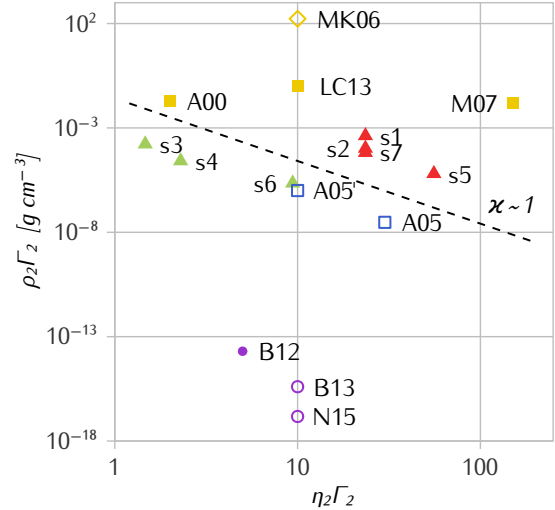


Figure 7. Parameters of counter-streaming plasma flows. A subset of simulations (this paper, red triangles s1, s2, s5, s7) demonstrates copious pair production and significant synchrotron losses, whereas in the other simulations of this paper (green triangles s3, s4, s6) the positron yield is low and the energy of synchrotron photons does not much exceed the energy of magnetic field. These subsets evidently belong to the regions $\varkappa > 1$ (above the dashed line) and $\varkappa < 1$ (below it), respectively (for \varkappa see Eq. (45) and Table 1). A number of numerical models of GRBs (collapsars with neutrino-antineutrino annihilation powered jets (yellow squares A00, LC13, M07), mergers (hollow blue squares A05 and A05'), a collapsar with Blandford–Znajek powered jet (a hollow yellow diamond MK06) found in the literature, as well as the estimated properties of a tidal disruption event leading to jet formation (solid circle B12) and blazars (hollow circles B13 and N15) are also shown (see text for details).

ing matter. In that process, strong jets are generated due to energy deposition in the progenitor star envelope within the cone region around the rotation axis of the star. This energy deposition can be associated with neutrino-antineutrino annihilation with subsequent heating and acceleration of the baryonic matter. The Weibel instability can rise either in internal shocks in the jets or external shocks with pre-explosive stellar wind or the star envelope. Note that in this model huge external pressure that accelerates the jets is often associated not with the ion temperature but mostly with radiation, hence we use $\eta \sim 1$ for this model. Note that such assumption neglects e^+e^- pairs produced by neutrino-antineutrino annihilation and contributing to the plasma density, hence the parameter \varkappa given for the collapsar models below is rather underestimated.

In the simulations based on the MacFadyen & Woosley model (Aloy et al. 2000) with the energy deposition

of the order of 10^{50} – 10^{51} erg, the jet breaking-out the progenitor star has the rest-mass density about 10^{-1} g cm $^{-3}$, the temperature $\eta \sim 1$ and the Lorentz factor $\Gamma \sim 5$, while the envelope of the star is motionless and has density about 1 g cm $^{-3}$ (see dotted lines in Fig. 2 from Aloy et al. (2000)). In the center-of-momentum reference frame, the Lorentz factor of the less dense flow (the jet) can be estimated as follows: $\Gamma_2 \sim 2$, while the rest-mass density and thermal energy of ions, obviously, are the same, $\rho_2 \sim 10^{-2}$ g cm $^{-3}$, $\eta_2 \sim 1$. These parameters yield $\varkappa \approx 2.5$ and are shown as yellow square A00 in Fig. 7.

In the two-dimensional simulation of Morsony et al. (2007) adhering the MacFadyen & Woosley collapsar model and a power law stellar envelope model, the energetic jet ($\Gamma \approx 300$, $\rho \sim 10^{-4}$ g cm $^{-3}$, see color version of Fig. 3 from Morsony et al. (2007)) breaks out the star envelope ($\rho \sim 10^{-1}$ g cm $^{-3}$) that provides favorable conditions for the extreme Weibel instability ($\Gamma_2 \sim 150$, $\eta_2 \sim 1$, $\rho_2 \sim 10^{-4}$ g cm $^{-3}$, $\varkappa \approx 10^3$, see the red square M07 in Fig. 7). In the further development of this model (three-dimensional simulation with more realistic stellar progenitor, see López-Cámara et al. (2013)) the parameters of jet breaking out the progenitor star (at $t = 4.2$ s) are slightly different: the jet has $\Gamma \approx 10$ and $\rho \sim 10^{-2}$ g cm $^{-3}$, and the envelope has $\rho \sim 1$ g cm $^{-3}$ (see the green lines in Figs. 4 and 6 of López-Cámara et al. (2013)). These parameters yield $\Gamma_2 \sim 10$ and $\rho_2 \sim 10^{-2}$ g cm $^{-3}$ (shown in Fig. 7 as LC13 yellow square) which, together with $\eta \sim 1$, is above the threshold $\varkappa \sim 1$ ($\varkappa \approx 60$).

Short GRBs are not linked with supernova explosions, and it is proposed that mergers (neutron star – neutron star or neutron star – black hole mergers) could be the source of such bursts. It implies lower density of the ambient and the jet plasma, and greater Lorentz factor of jets in general (Aloy et al. 2005). For instance, in the simulation B01 at time 0.5 s (see Figs. 25 and 26 of Aloy et al. (2005)), the Lorentz-factor of the jet head is $\Gamma \approx 1000$, and its rest-mass density is only $\rho \sim 10^{-9}$ g cm $^{-3}$. Assuming the internal shock in such jet having $\Gamma_2 \sim \Gamma^{1/2} \approx 30$ (A05 hollow blue square in Fig. 7), we obtain $\varkappa \approx 0.2$. Earlier, i.e. at time 0.1 s, the head of the jet has the Lorentz-factor $\Gamma \sim 100$ and density $\rho \sim 10^{-7}$ g cm $^{-3}$ (see Figs. 15 and 16 in Aloy et al. (2005)). The corresponding parameters of internal shock with $\Gamma_2 \sim \Gamma^{1/2} \approx 10$ again are not favorable for pair production during the Weibel instability ($\varkappa \approx 0.2$) and are shown as A05' hollow blue square in Fig. 7.

Another model of jet formation in long GRB engines connects it with the Blandford–Znajek mechanism of energy extraction from rotating black hole (Blandford &

Znajek 1977), and predicts the formation of a magnetically driven outflow McKinney (2006) (i.e, an outflow with magnetic pressure dominating over particle pressure and Poynting flux dominating over the flux of the particle energy). This model allows one to estimate the plasma density if the GRB luminosity and the mass of the central black hole is known (see the next subsection for details). For example, for a black hole with mass $M_{BH} = 10M_\odot$ (where M_\odot is the solar mass) and the overall jet luminosity $L_j = 10^{50}$ ergs $^{-1}$ that is typical for long GRBs (Piran 1999) one can obtain huge density $\rho_2 \sim 17$ g cm $^{-3}$ that together with $\Gamma_2 \approx 10$ leads to $\varkappa \sim 10^3$ and is shown with MK06 hollow yellow diamond in Fig. 7.

Thus, the pair production regime of the Weibel instability potentially can be reached in long gamma-ray bursts associating with collapse of massive stars. Short gamma-ray bursts associating with merging of black holes or neutron stars presumably provides $\varkappa \lesssim 1$ and negligible rate of pair production in the magnetic field of collisionless shocks.

4.2. Supermassive black holes

It is generally believed that super massive black holes (SMBHs) drive energetic outflows in active galactic nucleus (AGNs) and blazars. However, a large value of Schwarzschild radius of SMBHs implies a low value of the plasma density and $\varkappa \ll 1$.

Swift J164449.3+573451 source, which is associated with a tidal disruption of a star by a dormant SMBH (Zauderer et al. 2011), is of a certain interest because the observable data allows one to estimate the jet parameters not far from, but quite near the black hole. Rapid time variability of the gamma-rays and X-rays requires a compact source with a characteristic size of $\lesssim 0.15$ AU ($\lesssim 2 \times 10^{12}$ cm) (Berger et al. 2012). More than 200 days of radio observations of the source let one obtain the jet properties at the distance $r_{rf} \sim 10^{18}$ cm from the black hole (Berger et al. 2012): $\Gamma \approx 5$ and $n(r_{rf}) \sim 1$ cm $^{-3}$. Assuming that the opening angle of the jet $\theta_j \sim 5^\circ$, the distance between the SMBH and the gamma- and X-ray source is $r_\gamma \sim (\tan \theta_j)^{-1} \times 0.15$ AU $\sim 2 \times 10^{13}$ cm that yields at this distance $n(r_\gamma) \sim n(r_{rf})r_{rf}^2/r_\gamma^2 \sim 2.5 \times 10^9$ cm $^{-3}$, hence $\rho_2 \sim 4 \times 10^{-15}$ g cm $^{-3}$. This value, together with $\Gamma_2 \approx 5$ and $\eta_2 \approx 1$, gives $\varkappa \sim 10^{-5}$. and is depicted as B12 violet circle in Fig. 7.

The parameters of blazar jets can be similarly found from radio observations and luminosity in all bands, and then can be continued up to the distance closer to the central black hole. The distance from the black hole r_γ , at which the internal shock and the Weibel insta-

bility rise, is crucial for a plasma density estimate and can be found as follows. First, r_γ is connected with the variability timescale t_{var} and the jet opening angle θ_j , $r_\gamma \sim ct_{var}(\tan\theta_j)^{-1}$. Second, the numerical hydrodynamical model of jet formation of McKinney (2006) which takes into account general relativity and is capable to model Blandford-Znajek mechanism of jet supply (Blandford & Znajek 1977), predicts that the magnetic pressure dominates in the jet from the region of jet formation up to the Alfvén surface at $r_A \sim 10\text{--}100 r_g$, where $r_g = 2GM_{BH}/c^2$ is the black hole Schwarzschild radius, M_{BH} is the black hole mass and G is the gravitational constant. Beneath the Alfvén surface, the internal shocks are absent in the simulations of McKinney (2006), hence $r_\gamma \geq r_A \sim 100r_g$.

Let us assume that jet luminosity L_j is equal to the jet energy traveling through the jet cross-section at r_γ , and the particle energy becomes comparable with the energy of magnetic field here, hence

$$L_j \sim \pi r_\gamma^2 \rho c^3 \eta \Gamma^2 \tan^2 \theta_j, \quad (46)$$

Thus, in order to estimate ρ one should know M_{BH} , Γ and η . Relying on the simulations of McKinney (2006), we use $\Gamma \approx 10$ and $\theta_j \approx 5^\circ$ in the further estimations, additionally assuming $\eta \sim 1$.

In order to estimate parameters of internal shock nearest to the black hole of the famous blazar 3C273, we follow Böttcher et al. (2013); Zdziarski & Böttcher (2015). In the leptonic model of Böttcher et al. (2013). $L_j \approx 1.3 \times 10^{46}$ erg s $^{-1}$ (see Eq. 5 and value of L_p in Table 2 wherein), and in Ref. Zdziarski & Böttcher (2015) the black hole mass is assumed to be $M_{BH} \approx 7 \times 10^9 M_\odot$, that yields $r_\gamma = 2 \times 10^{15}$ cm, $\rho \approx 4 \times 10^{-17}$ g cm $^{-3}$ and $\varkappa \sim 10^{-6}$ (see B13 hollow blue circle in Fig. 7). Note that the variability timescale $t_{var} \sim 1$ day gives a slightly higher value of $r_\gamma \sim 3 \times 10^{16}$ cm and even lower value of \varkappa .

The reported detection of gravitational lensing of the blazar PKS 1830-211 (Neronov et al. 2015) independently provides the size of the gamma-ray emitting region about $r_\gamma/\tan\theta_j \sim 10^{15}$ cm, that coincides fairly well with about 1 day variability timescale and 10–100 r_g for the central black hole (Neronov et al. 2015). Thus, we adopt $r_\gamma \sim 10^{16}$ cm that, together with luminosity $L_j \sim 3 \times 10^{45}$ erg s $^{-1}$, leads to $\rho \sim 1.5 \times 10^{-18}$ g cm $^{-3}$ and $\varkappa \sim 10^{-6}$ (see N15 violet hollow circle in Fig. 7).

Therefore, SMBHs provides outflows with very low plasma density and $\varkappa \ll 1$.

4.3. Collisions

Fig. 7 clearly demonstrates that copious emission of hard photons and pair production during Weibel insta-

bility rises if the plasma density is at least 10^{-8} g cm $^{-3}$. In such plasmas, electron-photon and electron-ion collisions can be important, and the corresponding cross-sections should be estimated.

Compton scattering cross-section in the center-of-momentum reference frame can be estimated as follows (Berestetskii et al. 1982):

$$\sigma_C \sim \frac{r_e^2}{\bar{\gamma}^2} \ln \bar{\gamma}, \quad (47)$$

where $r_e = e^2/(mc^2)$ is the classical electron radius, the electron and photon energies are approximately equal to each other and to $\bar{\gamma}mc^2$. Thus, the ratio of the free time $t_f^{(C)} = 1/n\sigma$ (the mean time between two scattering events of the same particle) to the Weibel instability timescale Λ_m^{-1} (36) is:

$$\Lambda_m t_f^{(C)} \sim \frac{\bar{\gamma}^{3/2} \lambda}{\ln \bar{\gamma} r_e} \gg 1 \quad (48)$$

for almost any realistic plasma density (here λ is the plasma wavelength).

Electron-proton scattering can be considered similarly. The momentum-transfer (transport) cross section σ_{mt} is determined mostly by events with little change in the particle directions, and formulas for electron scattering in a constant field can be used (Landau & Lifshitz 1975; Berestetskii et al. 1982; Landau & Lifshitz 1976):

$$\sigma_{mt} \approx \frac{8\pi r_e^2}{\gamma_0^2} \ln \frac{\theta_{max}}{\theta_{min}}, \quad (49)$$

where θ_{max} and θ_{min} are the maximum and minimum deflection angles of the electron trajectory, respectively, and γ_0 is the initial Lorentz factor of the scattered electron. In the limit $\theta \ll 1$, the angles can be estimated as (Landau & Lifshitz 1975)

$$\theta \approx \frac{2r_e}{\gamma_0 r_0}, \quad (50)$$

where r_0 is the impact parameter. The minimal deflection angle θ_{min} can be estimated using the Debye length $r_D \sim c\bar{\gamma}^{1/2}/\omega_p$, and, as far as the electron de Broglie wavelength is smaller than the proton size ($\sim r_e$) and if $\gamma_0 \gtrsim \hbar c/e^2 \approx 137$, the maximal deflection angle can be estimated using the proton size. Therefore, we estimate the momentum-transfer cross-section as follows:

$$\sigma_{mt} \sim \frac{8\pi r_e^2}{\gamma_0^2} \ln \frac{\lambda \bar{\gamma}^{1/2}}{r_e}, \quad (51)$$

and the ratio of the corresponding timescale $t_f^{(ei)}$ to the timescale of the Weibel instability (36) as follows:

$$\Lambda_m t_f^{(ei)} \sim \frac{\lambda}{r_e} \bar{\gamma}^{3/2} \ln^{-1} \frac{\bar{\gamma}^{1/2} \lambda}{r_e}, \quad (52)$$

This ratio is smaller than $\Lambda_m t_f$ by a logarithmic factor of the order of 10, thus $\Lambda_m t_f^{(ei)}$ is also much greater than unity for almost all plasma parameters.

The characteristic timescale of electron energy losses caused by bremsstrahlung is about the timescale of e^+e^- pair production by a photon colliding with a proton (Berestetskii et al. 1982), and is the following:

$$\Lambda_m t_f^{(b)} \sim \frac{1}{\alpha \bar{\gamma}^{1/2} \ln 2 \bar{\gamma} r_e} \lambda, \quad (53)$$

where $\bar{\gamma}$ is the Lorentz factor of the emitting electron or the energy of the photon producing e^+e^- pair, normalized to mc^2 . For the density $\rho \sim 10^{-4} \text{ g cm}^{-3}$ and $\bar{\gamma} = 1.8 \times 10^4$ providing $\varkappa \sim 1$, we have $\Lambda_m t_f^{(b)} \sim 10^8$.

Therefore, for the parameters of interest the effect of collisions are negligible on the Weibel instability timescale. However, at least the scale $ct_{f,b}$ is less than the size of a gamma-ray emitting region in the collapsar model of GRBs (r_γ is less or about 1 light second for a $\nu\bar{\nu}$ -annihilation driven jet and $r_\gamma \sim 10^7 \text{ cm}$ for a jet driven by Blandford–Znajek mechanism). Namely, for a photon density of the order of $n_1 \sim n_2$, and $\rho_{1,2} \sim 10^{-4} \text{ g cm}^{-3}$, $\eta_{1,2} \sim 1$, $\Gamma_{1,2} \sim 10$ we obtain $ct_f^{(C)} \sim 10^{13} \text{ cm} \gg r_g$, $ct_f^{(ei)} \sim 10^{12} \text{ cm} \gg r_g$ and $ct_f^{(b)} \sim 10^6 \text{ cm} \ll r_g$.

Thereby the spectral energy distribution (SED) of photons would be drastically modified as they disappear in the e^+e^- photoproduction in collisions with nucleus. The cross-section of this process for high-energy photons ($\bar{\gamma} \gg 1$) depend logarithmically on the photon energy, and the threshold of the pair photoproduction $\bar{\gamma} \sim 1$ should be distinguished in the SED. Indeed, Fermi GBM data demonstrate that most SEDs of the detected GRBs have a break in the power-law fit (Gruber et al. 2014) or maxima in the photon energy distribution Abdo et al. (2009) at 100–1000 keV. The maximal photon energy detected in GRBs (tens of GeV, see Ackermann et al. (2014); Abdo et al. (2009)) is about the energy of a proton with Lorentz factor about 100 that coincides well with the generally believed Lorentz factor of GRB jets. Anyway, the generation of observed high-energy photons hardly can be attributed to high-density shock-wave region because of complicated energy-temporal distribution of photons (Ackermann et al. 2014; Abdo et al. 2009). Moreover, blazars also emitting photons with energy $\sim 10 \text{ GeV}$ nevertheless they have no regions of high-density plasma (see Fig. 7) that implies other mechanisms of high-energy photons generation (e.g., comp-tonisation).

Thus, collisional effects are negligible on the timescale of Weibel instability, however, bremsstrahlung as well as pair production in photon-proton collisions should be

taken into account on a scale of gamma-ray emitting region of GRBs.

5. SUMMARY

The Weibel instability in hot and dense counter-streaming relativistic plasma flows is considered theoretically and numerically. The results include the following.

- (i) Due to relativistic pinch of angles, if the flows Lorentz factor $\Gamma \gg 1$, the instability scenario for hot plasma is the same as for cold one, namely current filaments elongated in the direction of the flows velocity, and the magnetic field focusing the filaments, are formed.
- (ii) At the linear stage of the instability transverse filament scale λ_m and the instability growth rate Λ_m can be estimated using Eqs. (35) and (36). For certain Lorentz factor of the flows Γ and proper flows temperature ($\propto \eta$) one can find $\Lambda_m \propto (\eta\Gamma)^{-1/2}$ and $\lambda_m \propto (\eta/\Gamma)^{1/2}$.
- (iii) Numerical simulations reveal that the generated magnetic field causes an efficient synchrotron emission by electrons, and the overall energy of the synchrotron photons can be much higher than the energy of the magnetic field.
- (iv) The criterion for judging copious pair production in Weibel instability is proposed (see Eqs. (42) and (45)). Moreover, fulfillment of this criterion also ensures that the energy of synchrotron photons is greater than the magnetic field energy (iii).
- (v) The considered effects become noticeable for plasma with very high value of the mean electron Lorentz factor, that leads to the timescale of collisional effects much larger than the instability timescale.
- (vi) In the framework of the collapsar model of long gamma-ray bursts, $\varkappa \gtrsim 1$ and even $\varkappa \gg 1$ can be reached for the interaction of the jet with the progenitor star envelope, or for internal shock in the jet at the distance about 100 Schwarzschild radii from the black hole (see Fig. 7).

The Weibel instability that leads to $\varkappa \gg 1$ should potentially modify the plasma parameters dramatically. The gamma-ray emission and the photon e^+e^- pair production would not stop until the mean particle energy becomes so low that $\varkappa \lesssim 1$. Therefore, in the shock region the plasma density can be increased much due to the pair production, that at the same time leads to

the decrease of the mean particle energy. The impact of this scenario on the GRBs models would be considered elsewhere.

6. ACKNOWLEDGEMENTS

This research was supported by the Russian Foundation for Basic Research (Grant No. 15-02-06079), by the Grants Council under the President of the Russian Federation (Grant No. MK-2218.2017.2) and by “Basis” Foundation (Grant No. 17-11-101).

We thank V. V. Kocharovsky for inspiring conversations and I. I. Artemenko for discussion of the effect of collisions.

REFERENCES

- Abdo, A. A., Ackermann, M., Arimoto, M., et al. 2009, *Science*, 323, 1688
- Ackermann, M., Ajello, M., Asano, K., et al. 2014, *Science*, 343, 42
- Aloy, M. A., Janka, H.-T., & Müller, E. 2005, *Astronomy and Astrophysics*, 436, 273
- Aloy, M. A., Müller, E., Ibáñez, J. M., Martí, J. M., & MacFadyen, A. 2000, *The Astrophysical Journal*, 531, L119
- Baier, V. N., Katkov, V., & Strakhovenko, V. 1998, *Electromagnetic processes at high energies in oriented single crystals* (Singapore: World Scientific)
- Berestetskii, V. B., Lifshitz, E. M., & Pitaevskii, L. P. 1982, *Quantum Electrodynamics* (New York: Pergamon)
- Berger, E., Zauderer, A., Pooley, G. G., et al. 2012, *The Astrophysical Journal*, 748, 36
- Blandford, R. D., & Znajek, R. L. 1977, *Monthly Notices of the Royal Astronomical Society*, 179, 433
- Böttcher, M., Reimer, A., Sweeney, K., & Prakash, A. 2013, *The Astrophysical Journal*, 768, 54
- Chevalier, R. A. 1998, *The Astrophysical Journal*, 499, 810
- Efimenko, E., Bashinov, A., Bastrakov, S., et al. 2017, "arXiv":1708.09636
- Elkina, N. V., Fedotov, A. M., Kostyukov, I. Y., et al. 2011, *Physical Review Special Topics - Accelerators and Beams*, 14, 054401
- Garasev, M., & Derishev, E. 2016, *Monthly Notices of the Royal Astronomical Society*, 461, 641
- Garasev, M. A., Korytin, A. I., Kocharovsky, V. V., et al. 2017, *JETP Letters*, 105, 164
- Grassi, A., Grech, M., Amiranoff, F., et al. 2017, *Physical Review E*, 95, 023203
- Gruber, D., Goldstein, A., Weller von Ahlefeld, V., et al. 2014, *The Astrophysical Journal Supplement*, 211, 12
- Huntington, C. M., Fiuza, F., Ross, J. S., et al. 2015, *Nature Physics*, 11, 173
- Landau, L., & Lifshitz, E. 1976, *Mechanics*, 3rd edn. (Butterworth-Heinemann)
- Landau, L. D., & Lifshitz, E. M. 1975, *The Classical Theory of Fields* (Oxford: Elsevier)
- Liu, X., Li, Y. T., Zhang, Y., et al. 2011, *New Journal of Physics*, 13, 093001
- López-Cámara, D., Morsony, B. J., Begelman, M. C., & Lazzati, D. 2013, *The Astrophysical Journal*, 767, 19
- MacFadyen, A. I., & Woosley, S. E. 1999, *The Astrophysical Journal*, 524, 262
- McKinney, J. C. 2006, *Monthly Notices of the Royal Astronomical Society*, 368, 1561
- Medvedev, M. V., Fiore, M., Fonseca, R. A., Silva, L. O., & Mori, W. B. 2005, *The Astrophysical Journal Letters*, 618,
- Morsony, B. J., Lazzati, D., & Begelman, M. C. 2007, *The Astrophysical Journal*, 665, 569
- Neronov, A., Vovk, I., & Malyshev, D. 2015, *Nature Physics*, 11, 664
- Nerush, E., & Kostyukov, I. Y. 2010, *Voprosy Atomnoj Nauki i Tekhniki*, 68, 3
- Nerush, E. N., Kostyukov, I. Y., Ji, L., & Pukhov, A. 2014, *Physics of Plasmas*, 21, 013109
- Nishikawa, K.-I., Niemiec, J., Hardee, P. E., et al. 2009, *The Astrophysical Journal Letters*, 698, L10
- Piran, T. 1999, *Physics Reports*, 314, 575
- Pukhov, A. 1999, *J. Plasma Physics*, 61, 425
- Saito, S., & Sakai, J.-I. 2004, *Physics of Plasmas*, 11, 859
- Serebryakov, D. A., Nerush, E. N., & Kostyukov, I. Y. 2015, *Physics of Plasmas*, 22, 123119
- Silva, L. O., Fonseca, R. A., Tonge, J. W., et al. 2003, *The Astrophysical Journal Letters*, 596, 4
- Soderberg, A. M., Chakraborti, S., Pignata, G., et al. 2010, *Nature*, 463, 513
- Spitkovsky, A. 2008, *The Astrophysical Journal Letters*, 682,
- Stockem, A., Fiuza, F., Bret, A., Fonseca, R. A., & Silva, L. O. 2014, *Nature Scientific Reports*, 4, 3934
- Vay, J.-L. 2008, *Physics of Plasmas*, 15, 056701
- Weibel, E. S. 1959, *Phys. Rev. Lett.*, 2, 83

Woosley, S. E., & MacFadyen, A. I. 1999, *Astron. Astrophys. Suppl. Ser.*, 138, 499

Zauderer, B. A., Berger, E., Soderberg, A. M., et al. 2011, *Nature*, 476, 425

Zdziarski, A. A., & Böttcher, M. 2015, *Monthly Notices of the Royal Astronomical Society: Letters*, 450, L21